Original Research Article

High-sensitivity pesticide detection on mango skin via terahertz spectroscopy with graphene oxide sensor

Xizu Wang*,†, Reuben J. Yeo†, Nan Zhang, Zhen Xiang Xing, Qiang Zhu, Karen Lin Ke*,†

*Institute of Materials Research and Engineering (IMRE), Agency for Science, Technology and Research (A*STAR), Singapore 138634, Singapore*

*** Corresponding author:** Xizu Wang, wangxz@imre.a-star.edu.sg; Karen Lin Ke, karen-kl@imre.a-star.edu.sg

† These authors contributed equally to this manuscript.

Abstract: Regular monitoring of pesticides in agricultural farmland is essential to prevent the misuse of toxic pesticide chemicals. As crop samples are typically disintegrated to extract the pesticide residue for chromatographic analysis, non-destructive techniques for pesticide monitoring are ideal for preventing the unwanted destruction of crops. This, however, requires analytical techniques that can detect trace pesticide amounts. Here, we show that terahertz (THz) spectroscopy in attenuated total reflection mode, combined with a low-cost graphene oxide (GO) plasmonic sensor, can be used for sensitive, fast, and non-destructive pesticide detection on mango skin. After the application of a pesticide solution onto the mango skin, the dried pesticide residue was transferred to the GO sensor by pressing it in contact with the mango skin surface. Due to the adsorption of the pesticide molecules onto the oxygen-rich GO surface, a signal in the THz range was obtained corresponding to the pesticide's chemical fingerprint. With this technique, pesticide surface concentrations of as low as 1 μg/cm^2 on mango skins can be detected.

Keywords: THz spectroscopy; pesticide monitoring; plasmonic sensors; agricultural crops; attenuated total reflectance

1. Introduction

The use of chemical pesticides is a modern agricultural practice to prevent the destruction of valuable food crops by pests, thereby improving crop yield and quality. Chemical pesticides are sprayed across large areas of plantations as aerosols that land on the crops or soil. Eventually, the pesticide can remain on the crop's surface as residue, can be absorbed by the plants themselves, or can be leached into groundwater beneath the soil. By their nature, chemical pesticides are poisonous to the organisms they are intended to eradicate. Pesticides are regulated by environmental and health authorities around the world, and pesticides in small amounts typically do not pose a risk to humans and the wider ecological habitat. However, excess dosages or the use of pesticides with high toxicities could lead to detrimental effects. For example, pesticides containing organochlorine compounds, such as lindane and dichlorodiphenyltrichloroethane (DDT), are carcinogenic and have largely been banned since the 1960s[1]. Nevertheless, because the high toxicity of organochlorine-based pesticides makes them highly effective in pest elimination, there have been reports as recent as 2019 that these pesticides are still being used in some parts of the world[2].

To prevent the misuse of pesticides, it is crucial for authorities to periodically monitor the dosage and use of restricted pesticides in agricultural regions. Conventionally, crop samples collected at random locations within an agricultural area are analyzed for their pesticide content via liquid or gas chromatography, where the crop is broken down with a solvent to extract the pesticide[3]. Alternatively, non-destructive analytical methods exist that do not require harvesting and destruction of crops. This is done by analyzing the dried pesticide residue that remains on the crop's surface as a benchmark of the pesticide content. A disadvantage of this approach is that the pesticide residue gradually gets removed from the crop's surface over time due to exposure

Received: 14 July 2023 Accepted: 1 September 2023 Available online: 27 September 2023

to weather elements. Therefore, the analytical techniques used in non-destructive pesticide monitoring need to be sensitive enough to detect trace amounts of pesticides.

In recent years, terahertz time-domain spectroscopy (THz-TDS) has been explored for chemical pesticide detection and analysis[4,5], in addition to its other applications in medical imaging and detection of biomolecules and toxic gases[6–8]. While the sensitivity of THz-TDS can be increased by using metamaterial sensors that enhance the pesticide's chemical fingerprint[9–11], they are expensive to fabricate. A more attractive alternative is to use sensors that can be fabricated into thin films. Previously, Xu et al.[5] have successfully used covalent-organic-framework (COF) thin films for THz sensing of pesticides. However, in their work, the pesticide was not studied in its dried residue state on the crop's surface but instead in the solution form that was left to dry on the sensor itself. Furthermore, the use of hazardous and flammable organic solvents, such as acetonitrile and benzaldehyde, to prepare the COF thin films restricts their scalability for mass production. On the other hand, graphene-based thin-film sensors can be prepared via liquid-phase exfoliation of graphite in aqueous solutions, which makes their production cheap, safe, and easily scalable[12–14]. Graphene-based materials support the propagation of surface plasmon polaritons that induce a strong plasmonic response in the THz range, thus contributing to their high detection sensitivity[15–20]. Furthermore, they also exhibit a high loading capacity for a variety of molecules due to the large surface area and conjugated 2D aromatic structure of graphene sheets that act as chemically active sites. This not only broadens the range of molecular species that can be detected but also enhances the responsiveness of the sensor to tiny changes in molecular concentrations[21,22]. Considering these advantages, graphene-based sensors have previously been explored for the detection of chemical pesticides in the solution form using electrochemical cells[23,24] and spectroscopic techniques, such as Raman or IR spectroscopy[25,26]. Among the various derivatives of graphene, graphene oxide (GO) can be synthesized in large volumes via simultaneous oxidation and exfoliation of graphite in water, commonly known as the Hummers method[13,14]. More importantly, the polar surface of GO is beneficial for the adsorption of organic pesticide molecules, especially those with polar moieties, onto the GO surface.

In this work, we demonstrate that pesticide residue on mango skins can be detected non-destructively and with high sensitivity via THz-TDS in an attenuated total reflectance (ATR) configuration with the aid of a GO sensor fabricated in our lab. Lidocaine (**Figure 1a**) was used as the pesticide chemical in this work[27,28]. To simulate pesticide application and adsorption onto mango skins, lidocaine solutions prepared at different concentrations were drop-cast onto the mango skin and left to dry. A portion of the dried lidocaine residue on the mango skin surface was then transferred onto the GO sensor for THz-TDS measurement. With the GO sensor, lidocaine surface concentrations down to 1 $\mu g/cm^2$ could be detected. The sensitivity of the GO sensor was attributed to the oxygen-rich GO surface that enhanced the chemical adsorption of lidocaine to GO.

2. Materials and methods

2.1. Materials

Lab-synthesized GO (hereon labeled as S-GO) was prepared via simultaneous exfoliation and oxidation of commercial graphite powder (7782-42-5, Alfa Aesar, 99.9% assay) according to the modified Hummers method with a pre-oxidation step to increase the number of oxygen-rich functionalities of the GO[13]. Oxidation of the graphite powder was carried out in a solution of potassium permanganate ($KMnO_4$; 7722-64-7, Junsei, Japan, 99.3%) acidified with sulfuric acid (H_2SO_4; 7664-93-9, Junsei, Japan, 95% assay) to a pH of 4–5, which was a comparably less acidic and hence more environmentally-friendly condition than that in commercial GO synthesis. Continued mixing of the graphite powder resulted in the formation of exfoliated S-GO flakes in the solution. The warm solution of S-GO was then filtered and washed with water to obtain the S-GO solution. Commercial GO (1034343-98-0, Graphenea SA, Spain), synthesized at pH 1.8–2.0, was used as a reference

for the characterization of S-GO. Undoped double-sided polished silicon (Si) wafers were diced into smaller pieces of 1 × 1 cm^2 and 2 × 2 cm^2, and these Si wafer pieces were used as the substrates for the GO sensor. The diced Si pieces were sonic-cleaned via a sequential sonication process in the following cleaning agents: a commercial detergent solution (Hellmanex® III, Hellma; 30 min), followed by de-ionized (DI) water (30 min), acetone (67-64-1, Sigma-Aldrich; 10 min), and isopropanol (67-63-0, Sigma-Aldrich; 10 min). After the final sonication step in isopropanol, the Si pieces were removed and dried under a flow of N_2. Solutions of lidocaine (137-58-6, Sigma-Aldrich) (**Figure 1a**) were prepared in ethanol (64-17-5, Sigma-Aldrich, 95% assay) to concentrations of 10–3000 mg/L. Fresh mangoes were purchased from the local supermarket. The skins were removed from the mangoes (**Figure 1b**) and diced into smaller pieces of approximately 1 × 1 cm^2 (**Figure 1c**). The mango skin pieces were thoroughly cleaned with soap and water to remove surface oils and contaminants and then dried with a paper towel.

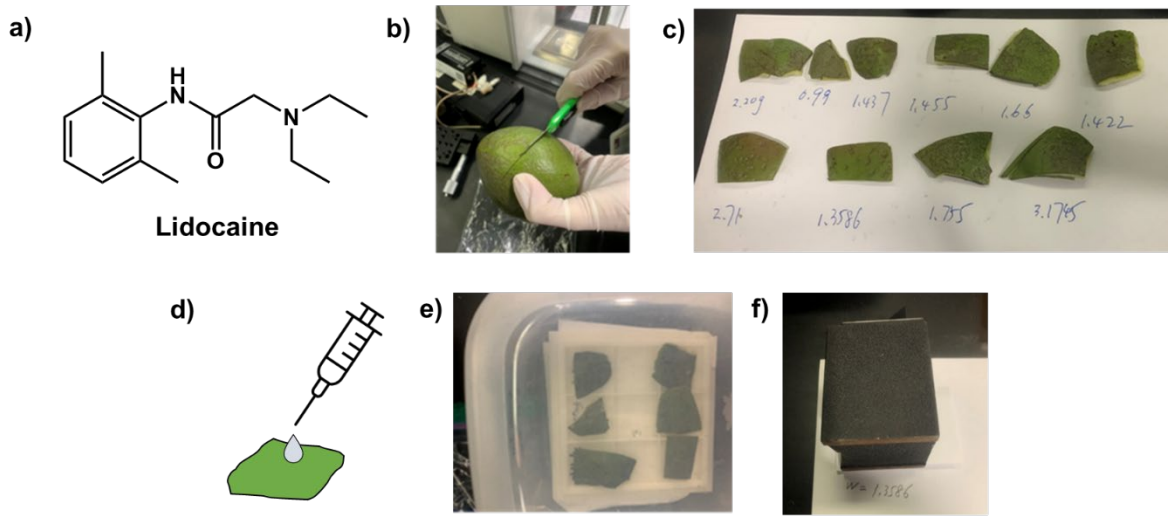

Figure 1. (a) Chemical formula of lidocaine. **(b–f)** Photographs and illustrations showing the procedure of lidocaine application on mango peels and transfer of lidocaine residue onto the GO sensor. **(b, c)** Mango peels were removed from the mango fruits and diced into smaller pieces of 1 × 1 cm^2, and the mango peel pieces were then cleaned with soap and water. **(d)** A solution of lidocaine was dropped onto the cleaned mango skin. **(e)** The mango skins were left in a closed box to allow the solvent to evaporate and prevent dust accumulation. **(f)** Dried lidocaine residue was transferred from the mango skin surface to the GO sensor surface using a press-transfer technique, which involved placing the GO sensor in contact with the mango skin surface and applying a 1kg weight on the back of the GO sensor.

2.2. Fabrication of GO sensor

The GO sensor was prepared by spin-coating an aqueous colloidal S-GO solution onto one side of the clean Si substrate. To prepare the colloidal S-GO solution, the S-GO powder was dispersed in water using mild sonication, as described in previous reports[13,29–31]. The concentration of the colloidal S-GO solution was ~2 $g.L^{-1}$. Prior to spin-coating, the Si surface on which the S-GO film was to be deposited was treated with UV-ozone for 10 min. Spin-coating was carried out at 2000 rpm. Subsequently, the S-GO film was dried on a hot plate at 110 ℃ for 10 min to obtain the GO sensor.

2.3. GO sensor characterization

All characterizations on the GO sensor were carried out on the spin-coated and dried S-GO film on Si. The morphology of the GO sensor was characterized via bright-field scanning-electron microscopy (SEM) (JEOL JSM-7001F) with a maximum electron-beam accelerating voltage of 5 kV. The GO sensor was imaged as is without depositing an additional conductive coating. The carbon bonding states of the GO sensor were characterized via X-ray photoelectron spectroscopy (XPS) (VG ESCALab, Thermo Fisher Scientific) equipped with a monochromatic Al-Kα source (1486.81 eV)[32]. Shirley background subtraction was performed on the

XPS C1s spectrum followed by peak fitting and quantification using the Origin software (OriginPro 2017, OriginLab, MA, USA). The carbon microstructure of the GO sensor was characterized via Raman spectroscopy in a confocal Raman microscope (WITec Alpha 300R) at room temperature using a 532nm laser with an excitation power of ~1 mW. The laser beam was focused onto the sample using a 100× objective lens. A dispersive grating with 600 grooves/mm (BLZ = 500 nm) was used to collect the Raman signals. The measured spectrum was baseline-corrected by subtracting the dark (background) spectrum from the measured spectrum. Peak fitting and quantification of the baseline-corrected spectrum were performed using the Origin software.

2.4. Transfer of lidocaine from mango skin surface onto GO sensor

To simulate the detection of dried pesticide residue from the agricultural crop surface, a lidocaine solution was applied to the mango skin surface and left to evaporate before the lidocaine residue was transferred to the GO sensor. Each concentration at 100 μL of the lidocaine solution was drop-cast directly onto a mango skin surface (**Figure 1d**) and stored in a closed box under an ambient condition for 1 h. This allowed the solvent to evaporate, while preventing dust accumulation on the mango skin surface during this time (**Figure 1e**). To transfer the dried lidocaine residue from the mango skin to the GO sensor, the GO sensor surface was placed in contact with the mango skin surface. A weight of 1 kg was then used to press the GO sensor down onto the mango skin surface (**Figure 1f**). The weight was left in this position for at least 12 h.

2.5. Lidocaine measurement via gas chromatography–mass spectrometry (GC-MS)

Gas chromatography–mass spectrometry (GC-MS) (Agilent 7890A) was used to verify the amount of lidocaine that was drop-cast on the mango skins. Mango skins that had been drop-cast with 10–380 mg/L ethanolic lidocaine solutions were cut into tiny pieces and immersed in 1.5 mL of dichloromethane (DCM) (75-09-2, Sigma Aldrich) for at least 12 h to completely dissolve the adsorbed lidocaine. The solution was then filtered before the GC-MS measurement to remove any mango skin pulp. The filtrate at 1 mL was used for GC-MS analysis. GC-MS instrument parameters and the oven temperature program for the lidocaine analysis are presented in **Table 1**. Based on the GC-MS settings, the peak corresponding to the species of the lidocaine molecule appeared at 26.42 min of retention time, and this was used as the primary measure of the amount of lidocaine present in the DCM solution. To determine the amount of lidocaine residue remaining on the mango skin surface after the press-transfer, mango skins after the press-transfer were dissolved in DCM and the filtered solution (without any mango skin pulp) was analyzed using GC-MS.

Table 1. GC-MS instrument parameters and oven temperature program used for measurement of lidocaine content on mango skins.

GC-MS setting	Parametric value
Instrumentation	Agilent 7890A chromatograph equipped with a 7693A auto-injector and a 5975C MSD mass detector
Column	HP-5, (5% Phenyl)-methylpolysiloxane, non-polar
Injector temperature	280 ℃
Injection volume	2 μL
Injection mode	Split
Column flow rate	1 mL/min
Split ratio	10:1
Carrier gas	Helium
Mass spectrometer mode	Electron impact positive ionization (EI+)
Scanning mass range	50 to 550 m/z
Oven temperature program	50 ℃ for 1 min, then 5 ℃/min ramp to 300 ℃, hold at 300 ℃ for 5 min

2.6. Terahertz time-domain spectroscopy (THz-TDS) measurements

THz radiation is an effective probe for pharmaceutical compounds, such as lidocaine, as the frequency range of THz radiation corresponds to the characteristic energies of their intermolecular and intramolecular vibrations. All THz-TDS measurements were performed in the ATR configuration in a commercial THz-TDS spectrometer (TPS Spectra 3000, TeraView Limited, Cambridge). The THz-TDS measurement setup is schematically illustrated in **Figure 2**.

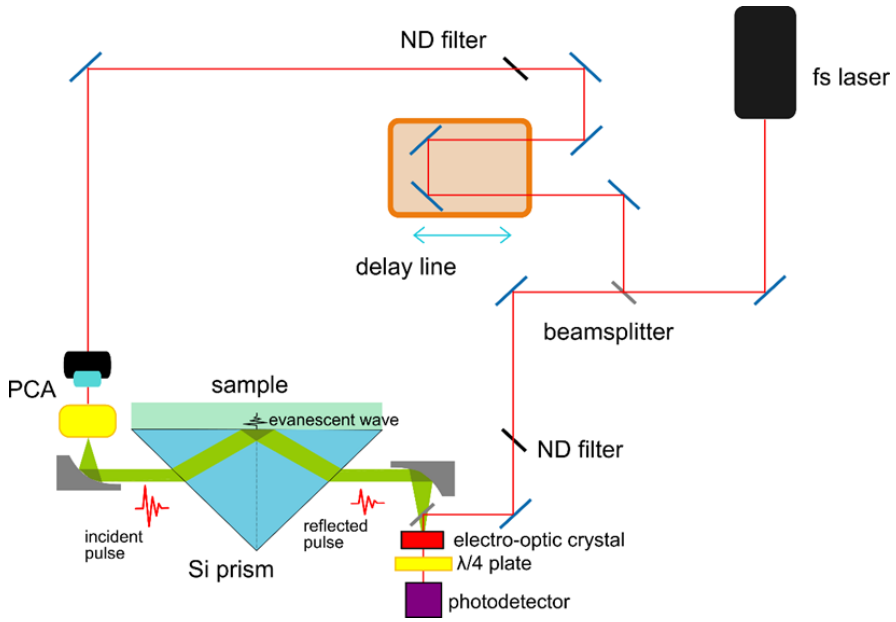

Figure 2. Schematic illustration of the THz-TDS setup for measurement in the attenuated total reflection (ATR) configuration. A pulsed THz beam incident at the prism-sample interface underwent total internal reflection and emitted an evanescent wave that interacted with the GO sensor surface. Energy absorbed by the adsorbed pesticide chemical on the GO sensor caused a change in the amplitude and phase of the reflected THz pulse, which was used as a measure of the pesticide content on the GO sensor.

Spectral data were acquired from each GO sensor by pressing it in contact with the single-crystal silicon ATR prism surface using a clamp. During the THz-TDS measurement, a pulsed laser beam with broadband frequencies in the THz region was transmitted into the Si ATR prism. The incident angle of the THz beam to the prism-sample interface was set at 57°, which resulted in a total internal reflection of the beam at the interface. A range of energies from the THz pulse were emitted as an evanescent electric field that penetrated the sample's sub-surface (approximately tens to hundreds of micrometers deep)[33] and the characteristic vibration energies were absorbed by the lidocaine present on the GO sensor. This in turn induced a change in the amplitude and phase of the reflected THz pulse, where the magnitude of the change in amplitude and phase can be used to determine the amount (concentration) of lidocaine present on the GO sensor. THz time-domain spectra were acquired for the bare GO sensor as a reference and then for the GO sensor with adsorbed lidocaine. Each spectrum comprised 1800 scans acquired at a rate of 30 scans per second for 60 s, with the frequency resolution set at 7.6×10^{-3} THz.

2.7. Terahertz time-domain spectroscopy (THz-TDS) data processing

Background subtraction of the measured ATR spectra was first performed on the measured THz time-domain spectrum by subtracting the signal obtained in the absence of a GO sensor. The background-subtracted spectrum was then normalized to the incident THz pulse to account for variations in incident pulse intensity. Through a fast Fourier transform (FFT) of the time-domain spectrum, the corresponding frequency-domain ATR spectrum could be derived. Assuming that the reflectance loss was absorbed by the GO sensor and

adsorbed lidocaine, the absorption coefficients at different frequencies could be calculated from the ATR data using established formulas (**Figure A1**)[34–36]. From this plot, it was revealed that the fingerprint absorption of lidocaine was in the 1.5–2.5 THz range.

The ATR intensity for the GO sensor with adsorbed lidocaine was derived by dividing the maximum ATR signal of the GO sensor with lidocaine in the 1.5–2.5 THz range by the magnitude of the ATR signal of pristine GO at the same frequency and then subtracting the result from unity. A total of eight different positions per sample were measured and the ATR reflection intensity was determined as the average intensity value measured from these eight positions.

2.8. Calibration of lidocaine concentrations via THz-TDS

Prior to the THz-TDS measurements of transferred lidocaine from mango skins, the GO sensors had to be calibrated with known amounts of lidocaine concentrations to correlate the ATR intensity to lidocaine concentration. Different concentrations of lidocaine in DCM solutions ranging from 10 mg/L to 3000 mg/L at 100 μL were drop-cast directly onto separate fresh GO sensor surfaces. The GO sensors were left to dry in a closed box under an ambient condition to allow for solvent evaporation, leaving behind only adsorbed lidocaine residue on the GO sensor. Subsequently, THz-TDS measurements were performed on these GO sensors. From THz-TDS frequency-domain spectra, the ATR intensity was determined for each lidocaine solution concentration to plot a calibration curve.

3. Results and discussion

3.1. Characterization of GO sensor

Before the drop-cast and the press-transfer, the pristine GO sensor was characterized to determine its quality after fabrication. The fabrication of macroscopic GO films and membranes from GO dispersions in solvents is well documented[37]. SEM imaging was performed to visualize the morphology of the GO sensor. It was evident from the low-magnification image that the S-GO film had a smooth morphology that conformed to the surface of the silicon substrate (**Figure 3a**). A closer observation of the SEM image also revealed the presence of wrinkles in the film, which spanned tens of micrometers across the surface. The wrinkling was more obvious in a magnified image of the S-GO film covering a particle sitting on the silicon surface (**Figure 3b**). This showed that the GO film was continuous and exhibited some elastic properties. The occurrence of wrinkling in a GO film formed from an aqueous GO dispersion had been observed previously and was attributed to the uncontrolled drying process of the film[38]. In addition, the morphology of S-GO thin films was found to be similar to those of commercial GO thin films formed from spin-coating aqueous dispersions of commercial GO powder on Si wafer substrates, as shown in side-by-side comparisons of their SEM images (**Figure A2**). Overall, these observations indicated the macroscopic uniformity and continuity of both the S-GO and commercial GO films across a large area of up to hundreds of square microns.

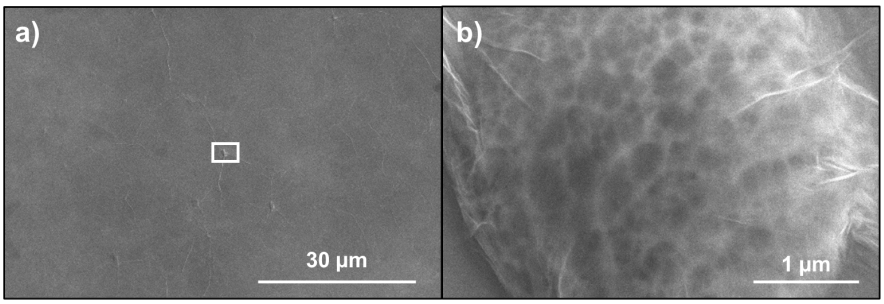

Figure 3. Scanning electron microscopy images of S-GO thin film after spin-coated onto silicon substrate and dried on hot plate to be made into GO sensor. Image **(b)** is the magnified image of the area bounded by the white rectangle in Image **(a)**.

XPS was performed primarily to investigate the degree of oxidation of the GO sensor. We deconvoluted the XPS C1s spectrum of the S-GO film into three constituent peaks of sp^2/sp^3 C-C (284.8 eV), C-O (286.9 eV), and O-C = O (288.4 eV) fitted with Gaussian components (**Figure 4a**)[39]. The integration of the peak areas showed that the S-GO film was highly oxidized, with a C-O fraction of 42.7%, O-C = O fraction of 9.3%, and sp^2/sp^3 C-C fraction of 48.0%. C-O groups typically arise from hydroxyl functions on the surface, whereas O-C = O groups mainly arise from carboxyl functions. Hence, we can conclude that the majority of oxygen-rich functionalities were hydroxyl groups. From the C1s spectra, the degree of oxidation for the S-GO film was determined to be ~52.0% based on the ratio of the C-O and O-C = O peak areas to the total C1s area. This was comparable to but slightly lower than the degree of oxidation of 55.2% for the commercial GO film as measured via XPS C1s in the same manner (**Figure 4b**). A summary of the constituent peak areas and degree of oxidation for S-GO and commercial GO films is presented in **Table 2**.

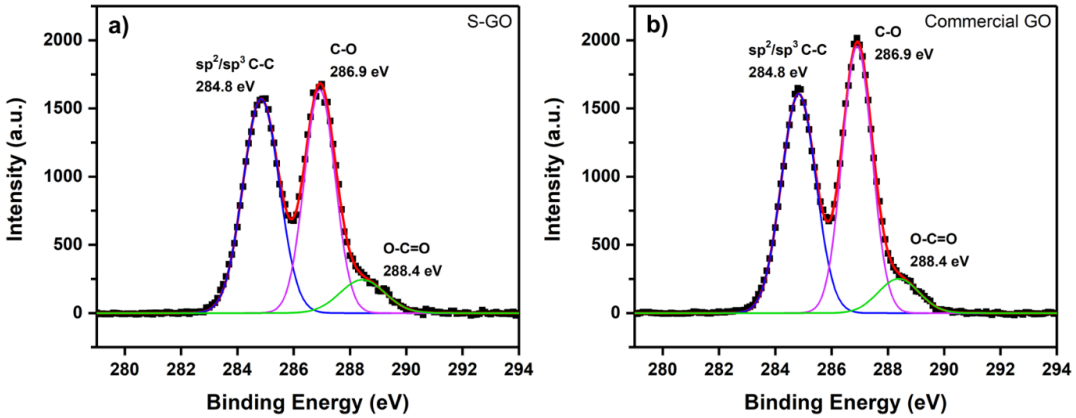

Figure 4. XPS high-resolution C1s spectra of GO films on silicon, fitted with three Gaussian: **(a)** S-GO and **(b)** commercial GO.

Table 2. Summary of key data extracted from XPS spectra of S-GO and commercial GO films on silicon.

Sample	Peak areas (a.u.)			Deg. of oxidation (%)
	sp^2/sp^3 C-C	C-O	O-C = O	
S-GO	2527.2	2244.1	488.5	52.0
Commercial GO	2471.4	2591.1	457.1	55.2

Next, the microstructure of the GO sensor was characterized via Raman spectroscopy. The Raman spectrum of GO film in the 1150–1850cm^{-1} wavenumber region was deconvoluted into four constituent peaks fitted with Lorentzian components ascribed to G, D, D′ and D″ bands (**Figure 5a**)[40] The G band at 1350 cm^{-1} arises from the Raman-active zone-center E_{2g} phonon mode of sp^2-bonded carbon. On the other hand, the D band at 1580 cm^{-1} is a defect-activated band ascribed to the presence of defects in the sp^2 carbon microstructure. The D′ band at 1613 cm^{-1}, like the D band, is another defect-activated band in sp^2 carbon materials, which becomes more obvious when the defect concentration is at a moderate level[41]. Finally, the D″ band at 1524 cm^{-1} is related to the fraction of the amorphous phase of sp^2 carbon in the material[42]. In comparison with typical commercial GO and graphite oxide materials (**Figure 5b**), the Raman spectrum of S-GO had a similar shape and D-to-G peak intensity ratio (I_D/I_G) of ~1.6[43], which leads us to conclude that the carbon microstructure of the S-GO film was similar to that of the commercial GO film. It should be noted that many papers reporting on the I_D/I_G ratio of GO gave a value of close to 1. However, in these works, the authors regarded the broad peak at ~1600 cm^{-1} to be a single G peak, instead of it being the sum of G and D′ peak components, and therefore calculated the I_D/I_G ratio based on the raw (unfitted) spectra[42, 44]. A summary of the Raman peak positions and I_D/I_G ratios for S-GO and commercial GO films is presented in **Table 3**.

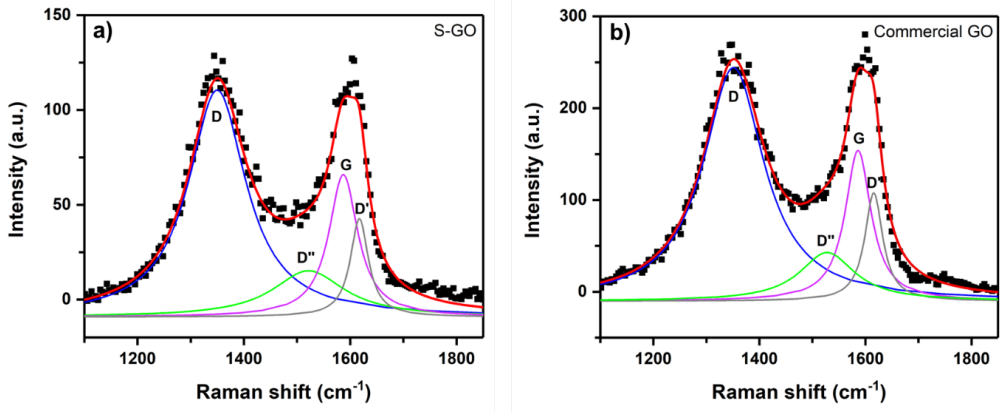

Figure 5. Raman spectra of GO films on silicon, fitted with four Lorentzian components that represent D, D″, G, and D′ peaks: **(a)** S-GO and **(b)** commercial GO.

Table 3. Summary of key data extracted from Raman spectra of S-GO and commercial GO films on silicon.

Sample	Peak positions (cm^{-1})				I_D/I_G
	D	D′	G	D″	
S-GO	1349.9	1521.6	1587.1	1617.3	1.59
Commercial GO	1351.3	1527.7	1586.2	1615.7	1.55

3.2. Measurement of lidocaine residue content on mango skins

GC-MS was used as a benchmark to determine the amount of drop-cast lidocaine on the mango skin before and after being press-transferred onto the GO sensor. Lidocaine concentrations of 10–380 mg/L were used for this experiment. During the drop-cast process, the area of the drop on the mango skin surface was approximately 1 cm^2. Knowing this allowed us to estimate the surface concentration of lidocaine on the mango skin surface. Within this concentration range, we performed a linear regression for both sets of data with a best-fit line that passed through the origin (**Figure 6**). After applying the press-transfer procedure, a significant decrease in GC-MS intensity was observed, demonstrating that a significant amount of lidocaine was successfully transferred to the GO sensor. The slopes of the two linear fits thus allowed us to extrapolate the approximate proportion of lidocaine transferred using the press-transfer procedure, which was calculated to be approximately 68% of the original amount of lidocaine dropped onto the mango skin.

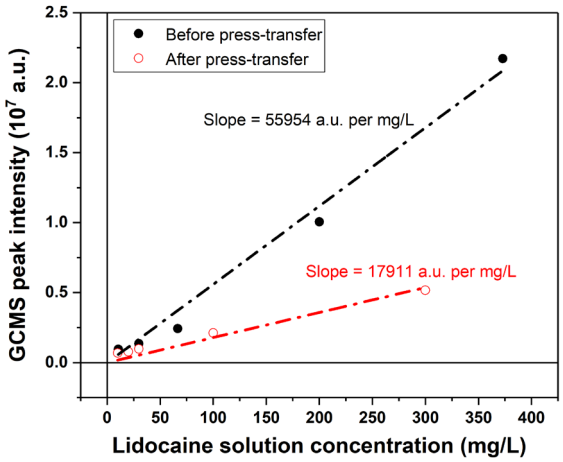

Figure 6. Relationship between concentration of drop-cast lidocaine solution on mango skins and peak intensity of lidocaine measured via gas chromatography–mass spectrometry (GC-MS) before and after press-transfer onto GO sensor. Linear regression was performed on both datasets to obtain best-fit line that passed through the origin.

To study the ATR intensity response with lidocaine concentration, we determined the ATR intensities from THz-TDS spectra measured on GO sensors with different concentrations of drop-cast lidocaine solutions ranging from 10 mg/L to 3000 mg/L (**Figure 7a**). We observed two distinct regimes in the trend of ATR intensity depending on the concentration of drop-cast lidocaine: one low-concentration regime for concentrations <350 mg/L (<35 μg/cm^2) and one high-concentration regime for concentrations ≥350 mg/L (≥35 μg/cm^2). The difference in the ATR intensity response in these two regimes can be attributed to the availability of oxygen-bearing functionalities on GO in the presence of different loadings of lidocaine molecules (**Figure 7b**). The plasmonic response of GO is sensitive to the chemical adsorption of molecules at the GO surface. At low concentrations (<350 mg/L), the abundance of adsorption sites on GO allowed almost all lidocaine molecules to be chemically adsorbed onto the GO surface, resulting in a highly sensitive ATR response with lidocaine concentration. This regime extended up to an intermediate concentration of 350 mg/L, where most of the adsorption sites on GO were fully occupied. As the lidocaine concentration increased above 350 mg/L, the first layer of adsorbed lidocaine molecules started to hinder the migration and attachment of subsequent molecules to the underlying GO adsorption sites. Since lidocaine molecules on the upper layers were not bound to the GO surface and did not contribute to the plasmonic response observed in the ATR signal, hence in this regime we see a smaller rise in ATR intensity with lidocaine concentration.

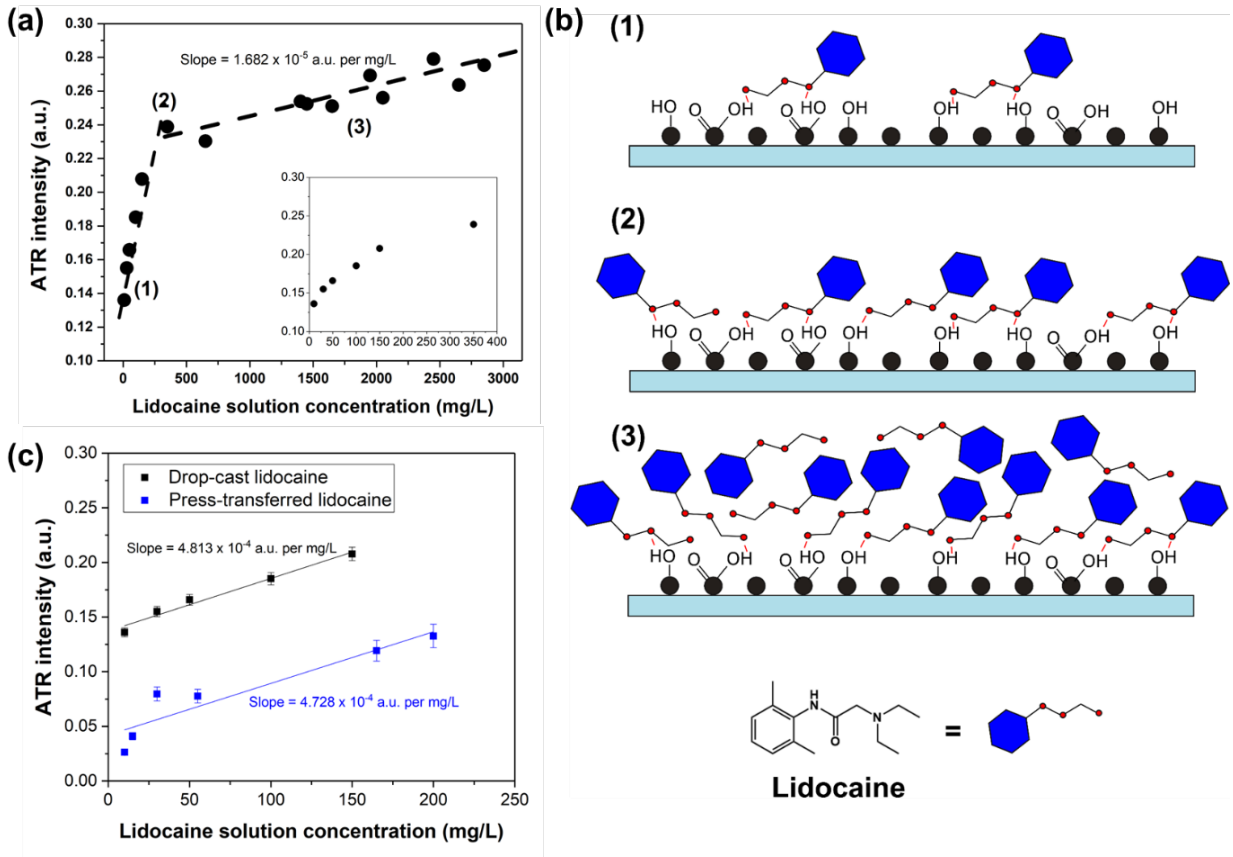

Figure 7. (a) Variation of ATR intensity with lidocaine solution concentration for drop-cast lidocaine on GO sensor. Two different regimes were observed, one at low lidocaine concentrations (< 350 mg/L) and one at high lidocaine concentrations (≥ 350 mg/L). The inset shows a clearer view of the data points in the low-concentration regime (10–350 mg/L). **(b)** Schematic illustrations showing the degree of saturation of the GO sensor surface by lidocaine molecules at (1) low concentration, (2) intermediate concentration, and (3) high concentration, as observed in **(a)**. **(c)** Comparison of ATR intensities for lidocaine solutions drop-cast directly onto GO sensor versus lidocaine solutions drop-cast on mango skins then press-transferred onto GO sensor for concentrations up to 200 mg/L.

For studying press-transferred lidocaine molecules from mango skins, we focus on the low concentration regime (10–200 mg/L) to probe the sensitivity of the THz-TDS technique for lidocaine detection. We fitted the ATR intensity data of drop-cast and press-transferred lidocaine to linear trendlines (**Figure 7c**). ATR peak intensities for press-transferred lidocaine samples were consistently lower than those of drop-cast lidocaine. This trend is unsurprising, since some lidocaine residue was expected to remain on the mango skin surface after the press-transfer process; this was also proven by GC-MS measurements. However, it can be observed that the ratio of ATR intensities between the two trendlines did not correspond to the ratio of 68% of lidocaine residue transfer to the GO sensor, as determined from GC-MS in **Figure 6**. This discrepancy can be attributed to the different ATR signal baselines for ethanolic lidocaine solutions directly drop-cast on the GO sensor versus press-transferred lidocaine from the mango skin. The difference in ATR signal baselines could be due to different surface concentration profiles of lidocaine developed on the two different surfaces after solvent drying, as well as the possibility of ethanol molecules from the drop-cast lidocaine solution that remain chemically adsorbed to the GO after drying. Still, at these low lidocaine concentrations, we could observe a variation in the ATR intensity as the lidocaine concentration was varied by tens of mg/L, which was an indication of the sensor's responsiveness. Furthermore, minute amounts of press-transferred lidocaine could still be detected on the GO sensor via THz-TDS ATR even for the lowest lidocaine solution concentration of 10 mg/L (surface concentration of 1 $\mu g/cm^2$) that was drop-cast on the mango skin[42]. These results show that the THz-TDS ATR technique in combination with a GO sensor is sensitive towards the detection of lidocaine detection at low concentrations and could therefore be translated to a high sensitivity for the detection of other pesticide chemicals.

4. Conclusion

We have successfully shown that THz-TDS in the ATR mode, in combination with a plasmonic GO sensor, can be used as a non-destructive method to measure low surface concentrations of pesticides of down to 1 $\mu g/cm^2$ on mango skins. GO was synthesized in our lab via simultaneous exfoliation and oxidation of commercial graphite in an aqueous medium under a condition that was less acidic than that of commercial GO synthesis, making the process more environmentally friendly and less hazardous, while maintaining its low cost and scalability of synthesis. The GO sensor was fabricated by spin-coating an aqueous dispersion of GO onto a polished silicon wafer surface to form a continuous and uniform GO thin film. Despite being synthesized non-commercially, the GO thin film was found to be comparable in quality to commercial GO thin films, with a similar carbon microstructure, degree of surface oxidation, and film uniformity. To simulate the application of pesticide onto a fruit skin surface, lidocaine solutions of different concentrations were drop-cast onto mango skins and left to dry. Subsequently, the dried pesticide residue was transferred onto the GO sensor using a press-transfer technique without having to destroy the mango skin. Due to the plasmonic enhancement offered by the GO sensor, THz-TDS in the ATR mode was found to be sensitive enough to detect press-transferred lidocaine adsorbed on the GO sensor even at the lowest lidocaine solution concentration of 10 mg/L, which corresponds to a lidocaine surface concentration of ~1 $\mu g/cm^2$ on the mango skin. Nevertheless, a high resolution of the GO sensor could be realized only in the low -concentration regime of lidocaine solution of <350 mg/L (surface concentrations <35 $\mu g/cm^2$), above which the resolution degraded due to saturation of the GO sensor at higher lidocaine amounts. This study demonstrates that THz sensors with a GO thin film can potentially be used for the non-destructive detection of trace amounts of pesticides on agricultural food crops for the purpose of pesticide monitoring and regulation. Future investigations on such THz sensors with a GO thin film may include applying the GO thin film onto flexible substrates that could better conform to the crop's surface, as well as studying their sensitivities to other types of pesticide chemicals (subject to license approval).

Author contributions

Conceptualization, KLK and XW; methodology, NZ and ZXX; software, KLK; validation, KLK and QZ; formal analysis, XW; data curation, KLK; writing—original draft preparation, RJY; writing—review and editing, RJY and XW; supervision, QZ. All authors have read and agreed to the published version of the manuscript.

Conflict of interest

The authors declare no conflict of interest.

References

1. Aktar WM, Sengupta D, Chowdhury A. Impact of pesticides use in agriculture: Their benefits and hazards. *Interdisciplinary Toxicology* 2009; 2(1): 1–12. doi: 10.2478/v10102-009-0001-7
2. Kayawe B. Widespread use of DDT for malaria control worries environmentalist. Available online: https://www.un.org/africarenewal/magazine/january-2022/widespread-use-ddt-malaria-control-worries-environmentalist (accessed on 14 February 2023).
3. González-Curbelo MÁ, Varela-Martínez DA, Riaño-Herrera DA. Pesticide-residue analysis in soils by the QuEChERS method: A review. *Molecules* 2022; 27(13): 4323. doi: 10.3390/molecules27134323
4. Hua Y, Zhang H. Qualitative and quantitative detection of pesticides with terahertz time-domain spectroscopy. *IEEE Transactions on Microwave Theory and Techniques* 2010; 58(7): 2064–2070. doi: 10.1109/TMTT.2010.2050184
5. Xu W, Wang S, Li W, et al. Pesticide detection with covalent-organic-framework nanofilms at terahertz band. *Biosensors and Bioelectroni*cs 2022; 209: 114274. doi: 10.1016/j.bios.2022.114274
6. Peng Y, Shi C, Zhu Y, et al. Terahertz spectroscopy in biomedical field: A review on signal-to-noise ratio improvement. *PhotoniX* 2020; 1: 12. doi: 10.1186/s43074-020-00011-z
7. Komatsu K, Iwamoto T, Ito H, Saitoh H. THz gas sensing using terahertz time-domain spectroscopy with ceramic architecture. *ACS Omega* 2022; 7(35): 30768–30772. doi: 10.1021/acsomega.2c01635
8. Lee SH, Choe JH, Kim C, et al. Graphene assisted terahertz metamaterials for sensitive bio-sensing. *Sensors and Actuators B: Chemical* 2020; 310: 127841. doi: 10.1016/j.snb.2020.127841
9. Lee DK, Kim G, Kim C, et al. Ultrasensitive detection of residual pesticides using THz near-field enhancement. *IEEE Transactions on Terahertz Science and Technology* 2016; 6(3): 389–395. doi: 10.1109/TTHZ.2016.2538731
10. Qin G, Zou K, Li Y, et al. Pesticide residue determination in vegetables from western China applying gas chromatography with mass spectrometry. *Biomedical Chromatography* 2016; 30(9): 1430–1440. doi: 10.1002/bmc.3701
11. Ye Y, Zhang Y, Zhao Y, et al. Sensitivity influencing factors during pesticide residue detection research via a terahertz metasensor. *Optics Express* 2021; 29(10): 15255–15268. doi: 10.1364/OE.424367
12. Tyurnina AV, Tzanakis I, Morton J, et al. Ultrasonic exfoliation of graphene in water: A key parameter study. *Carbon* 2020; 168: 737–747. doi: 10.1016/j.carbon.2020.06.029
13. Hummers WS Jr, Offeman RE. Preparation of graphitic oxide. *Journal of the American Chemical Society* 1958; 80(6): 1339–1339. doi: 10.1021/ja01539a017
14. Yu H, Zhang B, Bulin C, et al. High-efficient synthesis of graphene oxide based on improved hummers method. *Scientific Reports* 2016; 6(1): 36143. doi: 10.1038/srep36143
15. Ju L, Geng B, Horng J, et al. Graphene plasmonics for tunable terahertz metamaterials. *Nature Nanotechnology* 2011; 6(10): 630–634. doi: 10.1038/nnano.2011.146
16. Ranjan P, Gaur S, Yadav H, et al. 2D materials: Increscent quantum flatland with immense potential for applications. *Nano Convergence* 2022; 9: 26. doi: 10.1186/s40580-022-00317-7
17. Chiu NF, Huang TY. Sensitivity and kinetic analysis of graphene oxide-based surface plasmon resonance biosensors. *Sensors and Actuators B: Chemical* 2014: 197: 35–42. doi: 10.1016/j.snb.2014.02.033
18. Cittadini M, Bersani M, Perrozzi F, et al. Graphene oxide coupled with gold nanoparticles for localized surface plasmon resonance based gas sensor. *Carbon* 2014; 69: 452–459. doi: 10.1016/j.carbon.2013.12.048
19. Wu T, Liu S, Luo Y, et al. Surface plasmon resonance-induced visible light photocatalytic reduction of graphene oxide: Using Ag nanoparticles as a plasmonic photocatalyst. *Nanoscale* 2011; 3(5): 2142–2144. doi: 10.1039/c1nr10128e
20. Mencarelli D, Nishina Y, Ishikawa A, et al. THz plasmonic resonances in hybrid reduced-graphene-oxide and graphene patterns for sensing applications 2017; 3(1), 89–96. doi: 10.1515/odps-2017-0011

21. Zhang X, Xiang D, Wu Y, et al. High-performance flexible strain sensors based on biaxially stretched conductive polymer composites with carbon nanotubes immobilized on reduced graphene oxide. *Composites Part A: Applied Science and Manufacturing* 2021; 151: 106665. doi: 10.1016/j.compositesa.2021.106665
22. Justino CIL, Gomes AR, Freitas AC, et al. Graphene based sensors and biosensors. *TrAC Trends in Analytical Chemistry* 2017; 91: 53–66. doi: 10.1016/j.trac.2017.04.003
23. Ananda Murthy HC, Gebremedhn Kelele K, Ravikumar CR, et al. Graphene-supported nanomaterials as electrochemical sensors: A mini review. *Results in Chemistry* 2021; 3: 100131. doi: 10.1016/j.rechem.2021.100131
24. Shao Y, Wang J, Wu H, et al. Graphene based electrochemical sensors and biosensors: A review. *Electroanalysis* 2010; 22(10): 1027–1036. doi: 10.1002/elan.200900571
25. Chi SC, Lee CL, Chang CM. Adsorption of pesticides, antibiotics and microcystin-lr by graphene and hexagonal boron nitride nano-systems: A semiempirical PM7 and theoretical HSAB study. *Crystals* 2022; 12(8): 1068. doi: 10.3390/cryst12081068
26. Pang S, Yang T, He L. Review of surface enhanced Raman spectroscopic (SERS) detection of synthetic chemical pesticides. *TrAC Trends in Analytical Chemistry* 2016; 85(Part A): 73–82. doi: 10.1016/j.trac.2016.06.017
27. Chinn C, Lund AE, Yim GKW. The central actions of lidocaine and a pesticide, chlordimeform. *Neuropharmacology* 1977; 16(12): 867–871. doi: 10.1016/0028-3908(77)90150-2
28. Lapied B, Grolleau F, Sattelle DB. Indoxacarb, an oxadiazine insecticide, blocks insect neuronal sodium channels. *British Journal of Pharmacology* 2001; 132(2): 587–595. doi: 10.1038/sj.bjp.0703853.
29. Cote LJ, Kim F, Huang J. Langmuir-blodgett assembly of graphite oxide single layers. *Journal of the American Chemical Society* 2009; 131(3): 1043–1049. doi: 10.1021/ja806262m
30. Cote LJ, Cruz-Silva R, Huang J. Flash reduction and patterning of graphite oxide and its polymer composite. *Journal of the American Chemical Society* 2009; 131(31): 11027–11032. doi: 10.1021/ja902348k
31. Kim J, Cote LJ, Kim F, et al. Graphene oxide sheets at interfaces. *Journal of the American Chemical Society* 2010; 132(23): 8180–8186. doi: 10.1021/ja102777p
32. Carvalho A, Costa MCF, Marangoni VS, et al. The degree of oxidation of graphene oxide. *Nanomaterials* 2021; 11(3): 560. doi: 10.3390/nano11030560
33. Obradovic J, Newnham DA, Taday PF. Attenuated total reflection explores the terahertz region. Available online: https://www.americanlaboratory.com/913-Technical-Articles/1457-Attenuated-Total-Reflection-Explores-the-Terahertz-Region/ (accessed on 9 February 2023).
34. Holm RT, Palik ED. Thin-film absorption coefficients by attenuated-total-reflection spectroscopy. *Apploed Optics* 1978; 17(3): 394–403. doi: 10.1364/AO.17.000394
35. Hirori H, Yamashita K, Nagai M, Tanaka K. Attenuated total reflection spectroscopy in time domain using terahertz coherent pulses. *Japanese Journal of Applied Physics* 2004; 43(10A): L1287. doi: 10.1143/JJAP.43.L1287
36. Lai WE, Zhang HW, Zhu YH, Wen QY. A novel method of terahertz spectroscopy and imaging in reflection geometry. *Applied Spectroscopy* 2013; 67(1): 36–39. doi: 10.1366/12-06713
37. Cruz-Silva R, Endo M, Terrones M. Graphene oxide films, fibers, and membranes. *Nanotechnology Reviews* 2016; 5(4): 377–391. doi: 10.1515/ntrev-2015-0041
38. Tardani F, Neri W, Zakri C, et al. Shear rheology control of wrinkles and patterns in graphene oxide films. *Langmuir* 2018; 34(9): 2996–3002. doi: 10.1021/acs.langmuir.7b04281
39. Gengenbach TR, Major GH, Linford MR, Easton CD. Practical guides for X-ray photoelectron spectroscopy (XPS): Interpreting the carbon 1s spectrum. *Journal of Vacuum Science & Technology A* 2021; 39(1): 013204. doi: 10.1116/6.0000682
40. Lee AY, Yang K, Anh ND, et al. Raman study of D* band in graphene oxide and its correlation with reduction. *Applied Surface Science* 2021; 536: 147990. doi: 10.1016/j.apsusc.2020.147990
41. Eckmann A, Felten A, Mishchenko A, et al. Probing the nature of defects in graphene by Raman spectroscopy. *Nano Letters* 2012; 12(8): 3925–3930. doi: 10.1021/nl300901a
42. López-Díaz D, López Holgado M, García-Fierro JL, Velázquez MM. Evolution of the Raman spectrum with the chemical composition of graphene oxide. *The Journal of Physical Chemistry C* 2017; 121(37): 20489–20497. doi: 10.1021/acs.jpcc.7b06236
43. Muzyka R, Drewniak S, Pustelny T, et al. Characterization of graphite oxide and reduced graphene oxide obtained from different graphite precursors and oxidized by different methods using Raman spectroscopy. *Materials* 2018; 11(7): 1050. doi: 10.3390/ma11071050
44. Claramunt S, Varea A, López-Díaz D, et al. The importance of interbands on the interpretation of the Raman spectrum of graphene oxide. *The Journal of Physical Chemistry C* 2015; 119(18): 10123–10129. doi: 10.1021/acs.jpcc.5b01590

Appendix

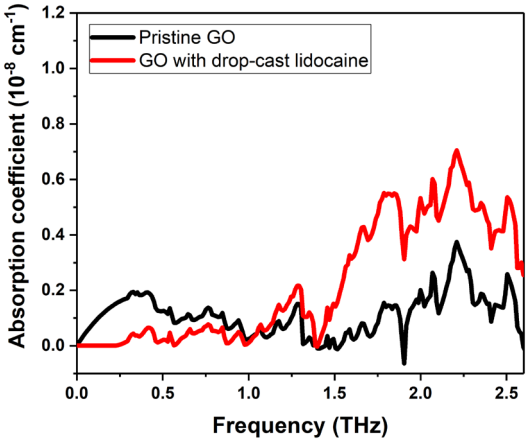

Figure A1. Variation of absorption coefficients with frequency obtained from ATR spectra measured on pristine GO and GO with drop-cast lidocaine (concentration 150 ppm). The fingerprint region of lidocaine on GO was found to be within the frequency range of 1.5–2.5 THz based on the larger absorption coefficients than that of the pristine GO in this range.

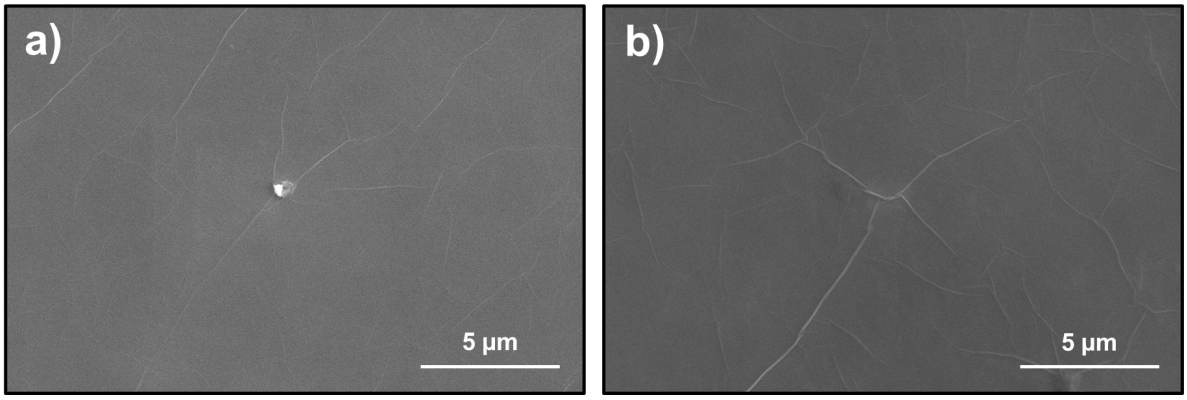

Figure A2. SEM images of GO spin-coated thin films on Si wafer substrates **(a)** S-GO and **(b)** commercial GO. The wrinkling of the GO films is a result of the uncontrolled drying process of the films on a hot plate after spin-coating. Nevertheless, the wrinkling clearly reveals the macroscopic continuity of both GO films in the SEM images.